SU(2) non-Abelian gauge field theory in one dimension on digital quantum computers

Natalie Klco,[*] Martin J. Savage,[†] and Jesse R. Stryker[‡]

Institute for Nuclear Theory, University of Washington, Seattle, Washington 98195-1550, USA

(Received 4 September 2019; revised manuscript received 24 December 2019; accepted 20 March 2020; published 21 April 2020)

A dynamical quantum simulation of SU(2) non-Abelian gauge field theory on a digital quantum computer is presented. This was enabled on current quantum hardware by introducing a mapping of the field onto a register of qubits that utilizes local gauge symmetry while preserving local constraints on the fields, reducing the dimensionality of the calculation. Controlled plaquette operators and gauge-variant completions in the unphysical part of the Hilbert space were designed and used to implement time evolution. The new techniques developed in this work generalize to quantum simulations of higher dimensional gauge field theories.

DOI: 10.1103/PhysRevD.101.074512

Non-Abelian gauge field theories play a central role in the description of the known forces of nature. Since the early 1970s, the strong interactions that define the nuclear forces and the dynamics of quarks and gluons in the early universe are known to emerge from an unbroken SU(3) local gauge symmetry, defining quantum chromodynamics (QCD) [1–3]. Similarly, the electroweak interactions are known to result from the spontaneous breaking of $\mathrm{SU}(2)_L \otimes \mathrm{U}(1)_Y$ local gauge symmetries [4–7]. Great success has been achieved in computing the properties and low-energy dynamics of hadronic systems using the numerical technique of lattice QCD [8,9] on the world's largest supercomputers. Current lattice QCD calculations at the physical quark masses have resulted from a sustained codevelopment effort over the last ∼50 years. Those developments began with calculations on small lattices, with unphysical quark masses, and with large lattice spacings using computers available during the 1970s [9]. While good progress is being made in designing Hilbert spaces for [10–28], creating detailed hardware-specific proposals for [29–44], and implementing [45–50] quantum field theories on quantum devices, non-Abelian gauge theories have not yet been simulated on today's limited and noisy hardware. It is in the spirit of the early days of lattice gauge theory that we develop an improved algorithm to evolve a string of SU(2) plaquettes, and use it to simulate a non-Abelian gauge field theory on IBM's digital quantum hardware.

The Hamiltonian formulation of lattice gauge theories [51] includes exponentially-large sectors of unphysical [52] Hilbert space in order to maintain spatially-local interactions while satisfying gauge constraints. The hardware error rates and gate fidelities of current NISQ-era [53] quantum devices, and the lack of error correction capabilities, allow quantum states to disperse into these unphysical sectors. To avoid such dispersion, previous quantum simulations of lattice gauge theories have employed various procedures to remove the unphysical Hilbert space from the embedding onto quantum devices [45–47,50,54]. However, these techniques do not scale efficiently, and a generic description for multidimensional lattices with nontrivial gauge groups in terms of only local, physical degrees of freedom is not currently known. A variety of approaches for quantumly simulating gauge theories are being pursued—reformulating the interactions, lattice structure, and degrees of freedom by designing Hilbert space bases of group elements, Schwinger bosons, duality transformations, loop variables, tensor networks, and more [23,25,26,30,36,39,51,55–78]—often with the explicit goal of mitigating unphysical degrees of freedom. Reductions have been obtained by solving Gauss's law, which is related to loop formulations where the fundamental degrees of freedom are gauge invariant [58,64,79–89]. Proposed for both analog and digital quantum implementation, progress is being made toward using renormalization group methods to connect quantum link models [13,32,35,90–94] to continuum theories of importance [93,95–97]. Classical numerical explorations of truncation errors arising from gauge field digitization in lattice QCD calculations [25], and exploring the use of the crystal groups associated with SU(3) to discretize the gluon fields for quantum simulations have begun [28]. Here marks the introduction of an explicit quantum algorithm for digital implementation of dynamics with generalizable operator structures.

In this work, the angular momentum basis [51,55,56] is utilized, which is made computationally feasible on

[*]klcon@uw.edu
[†]mjs5@uw.edu
[‡]stryker@uw.edu

quantum devices by exploiting the local gauge symmetry to remove the angular momentum alignment variables. A similar reduction in degrees of freedom has been suggested to be an advantageous mapping for quantum simulations [18], and has been employed in calculations using matrix product states. The associated qubit mapping, along with the flexibility of the introduced *gauge variant completion* (GVC), has made possible the exploration of operator structures necessary for generalization to larger lattices and higher dimensions on current hardware. As an explicit example, time evolution of a one-dimensional string of two SU(2) plaquettes is implemented on IBM's Tokyo [98] quantum device with employed error mitigation techniques. The new mappings and techniques that we introduce here generalize to quantum simulations of gauge field theories in higher numbers of spatial dimensions.

The Hamiltonian of spatially-discretized Yang-Mills gauge theory is [51] (in lattice units)

$$\hat{H} = \frac{g^2}{2}\sum_{\text{links}}\hat{E}^2 - \frac{1}{2g^2}\sum_{\square}(\hat{\square} + \hat{\square}^\dagger) \tag{1}$$

where $\hat{E}^2$ is the local gauge-invariant Casimir operator, $\hat{\square}$ is the gauge-invariant plaquette operator contracting closed loops of link operators, and $\hat{\square} = \hat{\square}^\dagger$ for SU(2). On a square lattice, the single plaquette operator is

$$\hat{\square} = \sum_{\alpha,\beta,\gamma,\delta=-\frac{1}{2}}^{\frac{1}{2}} \hat{U}_{\alpha\beta}\quad \hat{U}_{\beta\gamma}\quad \hat{U}_{\gamma\delta}\quad \hat{U}_{\delta\alpha} \tag{2}$$

where $\hat{U}_{\alpha\beta}$ is a $j = 1/2$ link operator with definite starting and ending points oriented around a plaquette. In the limit of strong coupling, $g^2 \to \infty$, this Hamiltonian is dominated by the electric contributions and fluctuations between configurations of definite link angular momentum vanish. In weak coupling, the magnetic contributions dominate and a theory of dynamical loops emerges.

The angular momentum basis describes the quantum state of a generic link by its irreducible representation, j, and associated third-component projections at the left and right end of the link in the $\mathbf{2}$ and $\bar{\mathbf{2}}$ representations, $|j, m, m'\rangle \equiv |j, m\rangle \otimes |j, m'\rangle$, respectively. In one dimension, SU(2) lattice gauge theory can be spatially discretized onto a string of plaquettes (see Fig. 1). With periodic boundary conditions (PBCs), only three-point vertices contribute to such a plaquette chain. To form gauge singlets, components of the three links at each vertex are contracted with an SU(2) Clebsch-Gordan coefficient. While these coefficients are conventionally incorporated into the state space allowing plaquette operators to be localized to four active links, the qubit Hilbert space is more naturally structured as an unconstrained grid. Thus the Clebsch-Gordan coefficient at each vertex will be here included in the plaquette operator itself. This decision

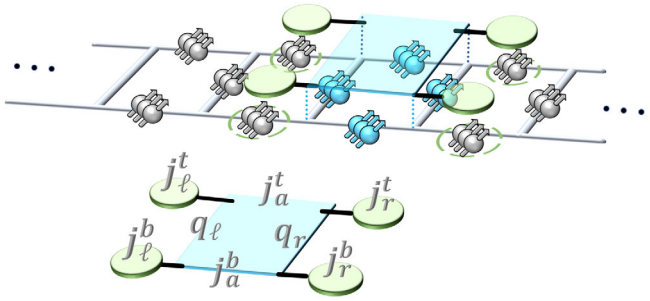

FIG. 1. (top) Diagram of the lattice distribution of $\lceil \log_2(2\Lambda_j + 1)\rceil$-qubit registers and the action of $\hat{\square}$ on SU(2) plaquettes in one dimension. $\hat{\square}$ operates on the four qubit registers in the plaquette and is controlled by the four neighboring qubit registers to enforce the Gauss's law constraint. (bottom) The plaquette operator with labeled angular momentum registers.

delocalizes the plaquette operator at the scale of immediately neighboring links as shown in Fig. 1, where the green, circular parts of the operator denote the dependence of the operator on the quantum state of qubits on neighboring links.

To calculate the plaquette operator, the state is first structured with Clebsch-Gordans at each vertex such that the wave function has the form

$$V \sim \sum_{b,c,e}\langle j_1, b, j_2, e|q, c\rangle |j_1, a, b\rangle \otimes |q, c, d\rangle \otimes |j_2, e, f\rangle, \tag{3}$$

where indices b, c, and e are located at the vertex. By focusing on a system with an even number of plaquettes, matrix elements of the arbitrary plaquette operator may be determined. The wave function of a lattice with an even number of plaquettes in one dimension with PBCs in the link angular momenta basis is

$$\begin{aligned}|\chi\rangle = \mathcal{N}\sum_{\{m\}}\prod_{i=1}^{L}&\langle j^t_i, m^t_{i,R}, j^t_{i+1}, m^t_{i+1,L}|q_i, m^t_{q_i}\rangle \\ &\times \langle j^b_i, m^b_{i,R}, j^b_{i+1}, m^b_{i+1,L}|q_i, m^b_{q_i}\rangle \\ &\times |j^t_i, m^t_{i,L}, m^t_{i,R}\rangle \otimes |j^b_i, m^b_{i,L}, m^b_{i,R}\rangle \otimes |q_i, m^t_{q_i}, m^b_{q_i}\rangle\end{aligned} \tag{4}$$

with $j_{L+1} = j_1$, $m_{L+1} = m_1$, and normalization $\mathcal{N} = \prod_i(\dim(q_i))^{-1}$ with $\dim(q) = 2q + 1$. Referring to the plaquette string's ladder structure, on links located as rungs of the ladder, angular momentum values are labeled by q. Thus, a plaquette string is created by two strings of j-type registers connected periodically by rungs of q-type registers. The contraction with Clebsch-Gordan coefficients at each vertex ensures the local gauge singlet structure required by Gauss's law. The link operator acts on the degrees of freedom at each end of a link and is a source of $j = 1/2$ angular momentum,

$$\hat{U}_{\alpha\beta}|j,a,b\rangle=\sum_{\oplus J}\sqrt{\frac{\dim(j)}{\dim(J)}}|J,a+\alpha,b+\beta\rangle \times\left\langle j,a,\frac{1}{2},\alpha\middle|J,a+\alpha\right\rangle\left\langle j,b,\frac{1}{2},\beta\middle|J,b+\beta\right\rangle, \quad (5)$$

which contains nonvanishing contributions only for $J=j\pm\frac{1}{2}$ [65]. By acting this operator on the above wave function of Eq. (4) and summing over alignment variables, that matrix elements of the plaquette operator in one dimension and in the tensor product basis of magnetic quantum numbers, j, are calculated to be

$$\begin{aligned}\langle\chi_{\ldots,j_\ell^{t,b},q_{\ell f},j_{af}^{t,b},q_{rf},j_r^{t,b},\ldots}|\hat{\square}|\chi_{\ldots,j_\ell^{t,b},q_{\ell i},j_{ai}^{t,b},q_{ri},j_r^{t,b},\ldots}\rangle &= \sqrt{\dim(j_{ai}^t)\dim(j_{af}^t)\dim(j_{ai}^b)\dim(j_{af}^b)}\\ &\times\sqrt{\dim(q_{\ell i})\dim(q_{\ell f})\dim(q_{ri})\dim(q_{rf})}\\ &\times(-1)^{j_\ell^t+j_\ell^b+j_r^t+j_r^b+2(j_{af}^t+j_{af}^b-q_{\ell i}-q_{ri})}\\ &\times\begin{Bmatrix} j_\ell^t & j_{ai}^t & q_{\ell i}\\ \frac{1}{2} & q_{\ell f} & j_{af}^t\end{Bmatrix}\begin{Bmatrix} j_\ell^b & j_{ai}^b & q_{\ell i}\\ \frac{1}{2} & q_{\ell f} & j_{af}^b\end{Bmatrix}\begin{Bmatrix} j_r^t & j_{ai}^t & q_{ri}\\ \frac{1}{2} & q_{rf} & j_{af}^t\end{Bmatrix}\begin{Bmatrix} j_r^b & j_{ai}^b & q_{ri}\\ \frac{1}{2} & q_{rf} & j_{af}^b\end{Bmatrix} \quad (6)\end{aligned}$$

where the indices $j_\ell^{t,b}, q_{\ell i}, q_{\ell f}, j_a^{t,b}, q_{ri}, q_{rf}$, and $j_r^{t,b}$ are used to indicate the j-values relevant for the single plaquette operator (as depicted in Fig. 1) and the brackets indicate Wigner's 6-j symbols. The four registers $j_{\ell,r}^{t,b}$ outside the plaquette are not modified by the action of the plaquette operator. However, their inclusion as control registers is necessary to maintain Gauss's law. The sums over alignment in each gauge-invariant space yield a dramatically reduced Hilbert space to be mapped onto a quantum device, characterized entirely by the $|j\rangle$'s (rather than the $|j,m,m'\rangle$'s [18]) incrementing naturally by half-integers. As a result, the Hilbert space dimension scales with the number of links, L, as $(2\Lambda_j+1)^L$—a small asymptotic savings in terms of qubit number, but an important savings for noisy devices where survival probabilities in the physical subspace are imperfect. This concept is here exemplified by embedding a four dimensional physical subspace into a sixteen dimensional computational space rather than into what would be a $\geq 5^4$-dimensional Hilbert space in the $|j,m,m'\rangle$ basis. The qubit representation of the periodic plaquette string is shown on the top panel of Fig. 1, where each link contains a $\lceil\log_2(2\Lambda_j+1)\rceil$-qubit register with Λ_j the angular momentum truncation per link.

Quantum circuits were devised for the plaquette operator with angular momentum truncation $\Lambda_j=1/2$. For time evolution beginning in the strong-coupling (empty) vacuum, the top and bottom j values are equivalent with this cutoff and the plaquette operator reduces to a five-qubit operator.

While the value of plaquette operator matrix elements connected to the physical Hilbert space are important for implementation of accurate time evolution, those within the unphysical space are not. Thus, significant freedom exists in designing the operator in the unphysical space to hardware-specifically optimize quantum computation. Operators with equivalent physical matrix elements but differing in their unphysical operation will be described as different gauge variant completions (GVCs) of the same physical operator. For example, here it is convenient to use a GVC within the set of Pauli operators to minimize the quantum gate resource requirements. Observing the plaquette operator matrix elements in Table I, states are connected when q_ℓ, j_a, and q_r experience a qubit inversion with a matrix element dependent on the j_ℓ, j_r-sector. Such a controlled operator is depicted schematically at the bottom of Fig. 1 (with top and bottom j's identified) and may be written as

$$\begin{aligned}\hat{\square}^{(1/2)} &= \Pi_0 XXX\Pi_0+\frac{1}{2}\Pi_0 XXX\Pi_1\\ &+\frac{1}{2}\Pi_1 XXX\Pi_0+\frac{1}{4}\Pi_1 XXX\Pi_1 \quad (7)\end{aligned}$$

with $\Pi_0=\frac{1}{2}(\mathbb{I}+Z)$ and $\Pi_1=\frac{1}{2}(\mathbb{I}-Z)$, the $j=0(\frac{1}{2})$ state mapped to quantum state $|0\rangle(|1\rangle)$, and the Hilbert spaces ordered as in the heading of Table I. With this GVC, the plaquette Hamiltonian has 24 nonzero couplings between

TABLE I. Matrix elements of the $\Lambda_j=1/2$, Hermitian plaquette operator $\hat{\square}^{(1/2)}$, as calculated in Eq. (6) with $j_{\ell,a,r}^t=j_{\ell,a,r}^b$. All other matrix elements between physical states are zero.

$\langle j_{\ell f}q_{\ell f}j_{af}q_{rf}j_{rf}\vert\hat{\square}^{(1/2)}\vert j_{\ell i}q_{\ell i}j_{ai}q_{ri}j_{ri}\rangle$	
$\langle 00000\vert\hat{\square}^{(1/2)}\vert 0\frac{1}{2}\frac{1}{2}\frac{1}{2}0\rangle$	1
$\langle 000\frac{1}{2}\frac{1}{2}\vert\hat{\square}^{(1/2)}\vert 0\frac{1}{2}\frac{1}{2}0\frac{1}{2}\rangle$	$\frac{1}{2}$
$\langle\frac{1}{2}\frac{1}{2}000\vert\hat{\square}^{(1/2)}\vert\frac{1}{2}0\frac{1}{2}\frac{1}{2}0\rangle$	$\frac{1}{2}$
$\langle\frac{1}{2}0\frac{1}{2}0\frac{1}{2}\vert\hat{\square}^{(1/2)}\vert\frac{1}{2}\frac{1}{2}0\frac{1}{2}\frac{1}{2}\rangle$	$\frac{1}{4}$

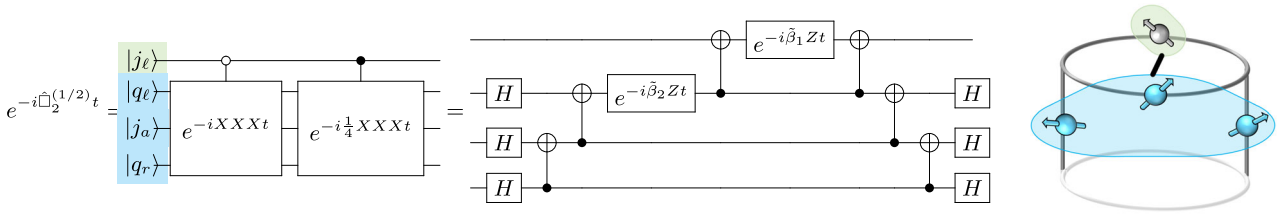

FIG. 2. Digital circuit implementation of the plaquette operator centered on j_a for a truncated lattice with $\Lambda_j = 1/2$, two plaquettes, and PBCs as depicted at the right. The angles $\tilde{\beta}$ defining this circuit are given in Eq. (B1) to be $\tilde{\beta} = (3/8, 5/8)$.

unphysical states that would otherwise vanish in the evaluation of Eq. (6) [99]. One possible digital qubit implementation of the associated time evolution operator with the GVC above is shown explicitly in Fig. 4 of Appendix B. As written, this operator acts equivalently throughout the one-dimensional string of plaquettes to implement time evolution of the lattice. We anticipate that the concept of GVC will play an important role in quantum simulations of quantum field theories in higher dimensions, and other physical systems with conserved quantities or constraints.

Specializing to the two-plaquette system with PBCs, only the matrix elements in the first and last rows of Table I remain. The second plaquette operator in the two-plaquette system reduces to the following four-qubit operator,

$$\hat{\square}_2^{(1/2)} = \Pi_0 XXX + \frac{1}{4}\Pi_1 XXX. \tag{8}$$

Digital implementation of this operator is shown in Fig. 2. The reduced linear combination structure defined by the first and fourth rows and columns of the matrix shown in Eq. (B1) produces the vector $\tilde{\beta}$ appearing in Fig. 2. A natural qubit representation of the electric operator is

$$\hat{H}_E^{(1/2)} = \frac{g^2}{2}\sum_{\text{links}}\frac{3}{4}\left(\frac{\mathbb{I} - Z}{2}\right), \tag{9}$$

including 12 nonzero elements in the unphysical Hilbert space.

Real-time evolution of two plaquettes with PBCs (see the right panel of Fig. 2) and truncation $\Lambda_j = 1/2$ has been here implemented on IBM's quantum device Tokyo, selected for its available connectivity of a four-qubit loop. The top panel of Fig. 3 shows time-evolved expectation values of the energy contributions from the first electric plaquette calculated with one and two Trotter steps [100]. The electric contributions, being localized in their measurement to the four-dimensional physical subspace, are well determined after a small number of samples. In contrast, measuring the energy contributions from the magnetic Hamiltonian requires increased sampling due to the operator's natural representation in the Pauli-X basis of the q_ℓ, j_a, and q_r qubit registers—distributing the wave function's amplitude throughout the Hilbert space. Results have been corrected for measurement error by the constrained inversion of a 16-dimensional calibration matrix informed by preparation of each of the 16 computational basis states prior to calculation. The resulting probabilities are linearly extrapolated in the presence of quantum controlled-NOT operation (CNOT gate), postselected within the gauge-invariant space, and renormalized. The linear extrapolation is informed by $r = 1, 2$, where $r = 1$ is the circuit in Fig. 2 and $r = 2$ stochastically inserts a pair of CNOTs accompanying each of the three CNOTs either in the first or second half of the plaquette operator. The

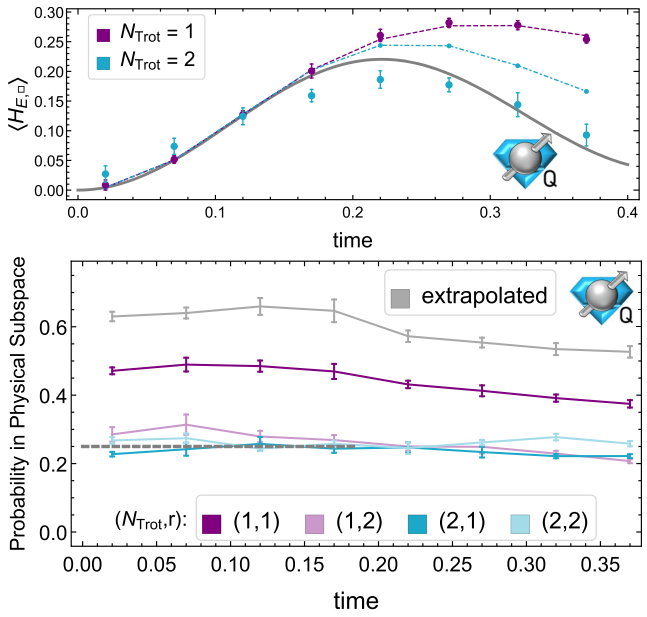

FIG. 3. (top) Expectation value of the electric energy contribution of the first plaquette in the two-plaquette lattice with PBCs and coupling $g^2 = 0.2$ computed on IBM's Tokyo. The dashed (purple) and dot-dashed(blue) lines are the $N_{\text{Trot}} = 1$, 2 Trotterized expectation values, while the thick gray line is the exact time evolution. (bottom) Measured survival probability to remain in the physical subspace for one and two trotter steps, N_{Trot}, and one and two r values indicating stochastically inserted $2r - 1$ CNOTs per CNOT in the digital implementation. Uncertainties represent statistical variation, as well as a systematic uncertainty estimated from reproducibility measurements. The icons (defined in Ref. [48]) denote computations performed on quantum devices.

combined noise and gate fidelity of the device were found to limit the ability to extrapolate further in CNOT noise, even with a single Trotter step. These error mitigation techniques have allowed calculation of the electric energy associated with the SU(2) gauge field to the precision obtained after a single Trotter step.

It is important to determine the feasibility of retaining gauge-invariant Hilbert spaces with near-term quantum hardware. For our calculations on IBM's Tokyo quantum device, before CNOT extrapolation, the $(N_{\mathrm{Trot}}, r) = (1, 1)$ measurements were found to remain in the gauge invariant space with a survival population of ∼45%, as shown in the bottom panel of Fig. 3. After linear extrapolation in the probabilities, this was increased to ∼65%, with survival population decreasing as evolution time increases. The survival population for $N_{\mathrm{Trot}} = 2$ was found to be ∼25%, consistent with loss of quantum coherence of a four-dimensional physical space embedded onto four qubits, precluding CNOT extrapolation. This observable is a diagnostic of the calculation. As it approaches the decorrelated limit (25%), CNOT extrapolations become less reliable, leading to the underestimate of systematic uncertainties in Fig. 3. Because neither the proposed qubit representation nor the subsequent Trotterization produce gauge-variant error contributions, the observed decay of population in the physical subspace is a measure of the device's ability to robustly isolate Hilbert subspaces. This is likely to be an essential capability for evolving lattice gauge theories and other systems with conserved quantities, as well as for quantum error correction.

When increasing Λ_j, the plaquette operator must be calculated and designed over 8 registers of qubits, each containing $\lceil \log_2 (2\Lambda_j + 1) \rceil$ qubits. The classical computational resources required to define this operator with Eq. (6) scales with the number of unique nonzero matrix elements, which is polynomial in Λ_j. When constructing the time evolution operator for $\Lambda_j > 1/2$, the combination of Trotterization and Pauli decomposition of the 4-register operators in $j_{\ell,r}$-controlled sectors generically generates interactions breaking gauge invariance [62,74,101]. While a unitary operator preserving gauge invariance exists, it will generically require an exponential amount of quantum resources to implement and classical resources to define. The breaking of gauge invariance will be important to control if this decomposition is used in future calculations.

For the simulated system, the SU(2) Hilbert space associated with each link and the spatial lattice are significantly truncated. This work represents an early step along the long road ahead for quantum simulations of gauge field theories. As Hamiltonian operators are local in such field theories, thoughtful design and optimization of quantum operators in small, classically manageable systems will impact the design and execution of future quantum simulations of larger dimensionality. The impact of the truncation on the continuous-field system of two plaquettes (for the value of g^2 used in this work) is presented in Table II of Appendix A. We find that the employed truncation of $\Lambda_j = 1/2$ leads to a ∼56% change to the ground state energy and a much larger change to the "glueball" mass. A larger value of g^2 would lead to smaller deviations in both quantities, as the system becomes more amenable to perturbative methods. At the selected value of g^2, where the system is nonperturbative, enlarging the simulation to include three qubits per link (a cutoff of $\Lambda_j = 7/2$), rather than one qubit per link ($\Lambda_j = 1/2$), causes these low-energy observables to become calculable with an accuracy exceeding 2% using the basis discussed in this paper. The fidelity of the ground state in the enlarged simulation is ∼90% with respect to the untruncated ground state. The convergence properties of this formulation of gauge theories, and others intended for quantum simulation, are important topics of future research.

Developing quantum computation capabilities for non-Abelian gauge field theories is a major objective of nuclear physics and high-energy physics research. We have presented the first quantum simulation of a non-Abelian gauge field theory on a digital quantum computer, which required the development of a number of new techniques. One of the challenges facing such calculations is that the mapping of the gauge theory onto the register of a digital quantum computer involves a digitization of the gauge fields. We have presented calculations of the dynamics of a one-dimensional SU(2) plaquette string with implementation on IBM's Q Experience superconducting hardware. This was made feasible by an improved mapping of the angular momentum basis states describing link variables and recognizing the utility of gauge-variant completions. Our design of the plaquette operator for digital quantum devices requires local control from qubit registers beyond the active plaquette. This key feature is expected to persist in future developments of quantum computing for gauge theories. Extension of this analytic reduction beyond one dimension is naturally suited to lattices with three-point vertices, but generalizes to n-point vertices and thus to quantum simulations in higher dimensions. Comparisons, at the level of explicit digital implementation, of this mapping with proposed alternatives will be of importance for realizing physically relevant quantum computations of non-Abelian gauge theories.

ACKNOWLEDGMENTS

We would like to thank David Kaplan, Indrakshi Raychowdhury and Erez Zohar for important discussions. We would also like to thank Donny Greenberg, the IBM quantum computing research group, and the ORNL Q Hub for informative discussions and facilitating access to the IBM quantum devices. We acknowledge use of the IBM Q for this work. The views expressed are those of the authors

and do not reflect the official policy or position of IBM or the IBM Q team. This work is supported in part by the U.S. Department of Energy, Office of Science, Office of Advanced Scientific Computing Research (ASCR) quantum algorithm teams program, under field work proposal number ERKJ333. We thank Raphael Pooser and ORNL collaborators with the U.S. Department of Energy, Office of Science, Office of Advanced Scientific Computing Research (ASCR) quantum Testbed Pathfinder program, under field work proposal number ERKJ335. This work was performed, in part, at the Aspen Center for Physics, which is supported by National Science Foundation Grant No. PHY-1607611. N. K., J. R. S., and M. J. S. were supported by the Institute for Nuclear Theory with DOE Grant No. DE-FG02-00ER41132 and Fermi National Accelerator Laboratory PO No. 652197. N. K. was supported in part by a Microsoft Research PhD Fellowship, and J. R. S. was supported in part by the National Science Foundation Graduate Research Fellowship Program under Grant No. DGE-1256082.

APPENDIX A: TWO PLAQUETTE HAMILTONIAN AND DATA TABLES

For the two-plaquette lattice with periodic boundary conditions and truncation $\Lambda_j = 1/2$, the Hamiltonian implemented in the full 16-dimensional Hilbert space with the gauge variant completion (GVC) discussed in the main text is

$$\mathcal{H}^{(1/2)} = \frac{1}{2g^2}\begin{pmatrix}
0 & 0 & 0 & 0 & 0 & 0 & 0 & -2 & 0 & 0 & 0 & 0 & 0 & -2 & 0 & 0 \\
0 & \frac{3g^4}{4} & 0 & 0 & 0 & 0 & -2 & 0 & 0 & 0 & 0 & 0 & -2 & 0 & 0 & 0 \\
0 & 0 & \frac{3g^4}{2} & 0 & 0 & -2 & 0 & 0 & 0 & 0 & 0 & 0 & 0 & 0 & 0 & -\frac{1}{2} \\
0 & 0 & 0 & \frac{9g^4}{4} & -2 & 0 & 0 & 0 & 0 & 0 & 0 & 0 & 0 & 0 & -\frac{1}{2} & 0 \\
0 & 0 & 0 & -2 & \frac{3g^4}{4} & 0 & 0 & 0 & -2 & 0 & 0 & 0 & 0 & 0 & 0 & 0 \\
0 & 0 & -2 & 0 & 0 & \frac{3g^4}{2} & 0 & 0 & -2 & 0 & 0 & 0 & 0 & 0 & 0 & 0 \\
0 & -2 & 0 & 0 & 0 & 0 & \frac{9g^4}{4} & 0 & 0 & 0 & 0 & -\frac{1}{2} & 0 & 0 & 0 & 0 \\
-2 & 0 & 0 & 0 & 0 & 0 & 0 & 3g^4 & 0 & 0 & -\frac{1}{2} & 0 & 0 & 0 & 0 & 0 \\
0 & 0 & 0 & 0 & 0 & -2 & 0 & 0 & \frac{3g^4}{2} & 0 & 0 & 0 & 0 & 0 & 0 & -\frac{1}{2} \\
0 & 0 & 0 & 0 & -2 & 0 & 0 & 0 & 0 & \frac{9g^4}{4} & 0 & 0 & 0 & 0 & -\frac{1}{2} & 0 \\
0 & 0 & 0 & 0 & 0 & 0 & 0 & -\frac{1}{2} & 0 & 0 & 3g^4 & 0 & 0 & -\frac{1}{2} & 0 & 0 \\
0 & 0 & 0 & 0 & 0 & 0 & -\frac{1}{2} & 0 & 0 & 0 & 0 & \frac{15g^4}{4} & -\frac{1}{2} & 0 & 0 & 0 \\
0 & -2 & 0 & 0 & 0 & 0 & 0 & 0 & 0 & 0 & 0 & -\frac{1}{2} & \frac{9g^4}{4} & 0 & 0 & 0 \\
-2 & 0 & 0 & 0 & 0 & 0 & 0 & 0 & 0 & 0 & -\frac{1}{2} & 0 & 0 & 3g^4 & 0 & 0 \\
0 & 0 & 0 & -\frac{1}{2} & 0 & 0 & 0 & 0 & 0 & -\frac{1}{2} & 0 & 0 & 0 & 0 & \frac{15g^4}{4} & 0 \\
0 & 0 & -\frac{1}{2} & 0 & 0 & 0 & 0 & 0 & -\frac{1}{2} & 0 & 0 & 0 & 0 & 0 & 0 & \frac{9g^4}{2}
\end{pmatrix}, \tag{A1}$$

with matrix elements of the four-dimensional physical subspace highlighted. For the chosen coupling of $g^2 = 0.2$, the ground state energy density per plaquette, through exact (classical) diagonalization, is calculated to be -3.5658 and the lowest energy gap (the observable associated with the "SU(2)-glueball" mass in the infinite volume limit) is calculated to be 7.4139. Numerical values for these low-energy observables with increasing Λ_j truncation are provided in Table II where percent-level convergence is achieved with three qubits per SU(2) gauge link.

For the quantum simulated system of two plaquettes with $\Lambda_j = 1/2$, the structure of the ground state wave function is

$$|\psi_{gs}\rangle = 0.6943\left|\square\,\square\right\rangle + 0.1666\left|\square\!\!\square\,\square\!\!\square\right\rangle + 0.4951\left(\left|\square\,\square\!\!\square\right\rangle + \left|\square\!\!\square\,\square\right\rangle\right). \tag{A2}$$

On each link, a single line corresponds to $j = 0$ and a double line corresponds to $j = 1/2$. The first electric, single plaquette operator in the full 16-dimensional space is diagonal

$$E^2_{\square_1} = \frac{g^2}{2}\mathrm{diag}\left(0, \frac{3}{4}, 0, \frac{3}{4}, \frac{3}{4}, \frac{3}{2}, \frac{3}{4}, \frac{3}{2}, \frac{3}{2}, \frac{9}{4}, \frac{3}{2}, \frac{9}{4}, \frac{9}{4}, 3, \frac{9}{4}, 3\right), \tag{A3}$$

TABLE II. Convergence of the ground state energy density and the energy gap to the first excited state, ΔE, of a two-plaquette SU(2) lattice with periodic boundary conditions as the truncation in the maximum excitation on any single link, Λ_j, is increased. Columns two and three show the number of states included in the basis of physical states below truncation and the number of nonzero matrix elements in the single plaquette operator.

Electric cutoff ($2\Lambda_j$)	Physical dimension	Plaquette matrix elements	GS energy density	ΔE
1	4	2	−3.5658	7.4139
2	27	31	−5.6437	2.0970
3	95	192	−6.8020	0.9285
4	304	790	−7.4258	0.5024
5	769	2494	−7.7527	0.3096
6	1784	6537	−7.9159	0.2220
7	3664	15028	−7.9921	0.1929
8	7081	31200	−8.0241	0.1885
9	12704	59894	−8.0355	0.1893
10	21823	107823	−8.0388	0.1900
11	35659	184268	−8.0396	0.1902
12	56420	301326	−8.0398	0.1902

TABLE III. Numerical values of the expectation value of the single electric plaquette energy contribution for time evolutions implemented with 1,2 Trotter steps as measured on IBM's quantum device Tokyo shown in the top panel of Fig. 3. Uncertainties represent statistical variation, as well as a systematic uncertainty estimated from reproducibility measurements.

$N_{\mathrm{Trot}} = 1$	
Time	$\langle H_{E,\square_l} \rangle$
0.02	0.009(9)
0.07	0.052(6)
0.12	0.127(7)
0.17	0.201(12)
0.22	0.261(10)
0.27	0.282(7)
0.32	0.278(8)
0.37	0.254(6)

$N_{\mathrm{Trot}} = 2$	
Time	$\langle H_{E,\square_l} \rangle$
0.02	0.027(14)
0.07	0.074(14)
0.12	0.124(14)
0.17	0.159(10)
0.22	0.186(15)
0.27	0.177(12)
0.32	0.144(20)
0.37	0.093(18)

TABLE IV. Survival probabilities in the physical subspace as measured on IBM's quantum device Tokyo shown in the bottom panel of Fig. 3. The label indicates (N_{Trot}, r) values. The linear extrapolation is determined by extrapolation of computational basis state probabilities in r for $N_{\mathrm{Trot}} = 1$. Uncertainties represent statistical variation, as well as a systematic uncertainty estimated from reproducibility measurements.

$(N_{\mathrm{Trot}}, r) = (1, 1)$	
Time	Survival probabilities
0.02	0.47(1)
0.07	0.49(2)
0.12	0.48(2)
0.17	0.47(2)
0.22	0.43(1)
0.27	0.41(2)
0.32	0.39(1)
0.37	0.37(1)

$(N_{\mathrm{Trot}}, r) = (1, 2)$	
Time	Survival probabilities
0.02	0.29(2)
0.07	0.31(3)
0.12	0.28(2)
0.17	0.27(1)
0.22	0.25(1)
0.27	0.25(2)
0.32	0.23(1)
0.37	0.21(1)

$(N_{\mathrm{Trot}}, r) = (2, 1)$	
Time	Survival probabilities
0.02	0.23(1)
0.07	0.24(2)
0.12	0.26(2)
0.17	0.24(1)
0.22	0.25(2)
0.27	0.23(2)
0.32	0.22(1)
0.37	0.22(1)

$(N_{\mathrm{Trot}}, r) = (2, 2)$	
Time	Survival probabilities
0.02	0.27(1)
0.07	0.27(1)
0.12	0.24(1)
0.17	0.26(1)
0.22	0.25(2)
0.27	0.26(1)
0.32	0.28(1)
0.37	0.26(1)

Linear extrapolation	
Time	Survival probabilities
0.02	0.630(14)
0.07	0.640(16)
0.12	0.659(25)
0.17	0.647(33)
0.22	0.572(17)
0.27	0.554(14)
0.32	0.535(17)
0.37	0.527(17)

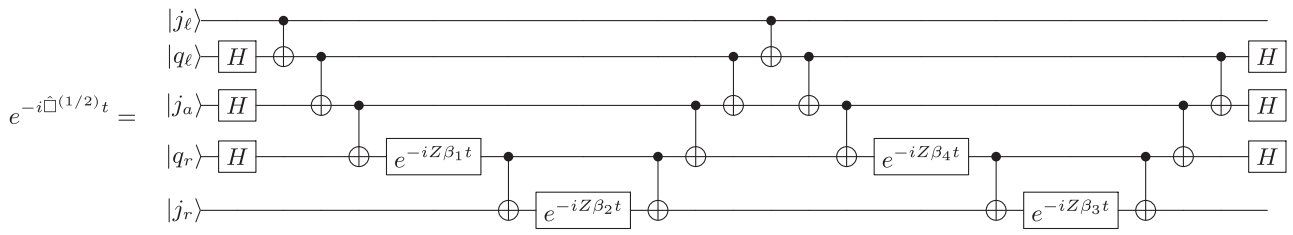

FIG. 4. Digital circuit implementation of the plaquette operator centered on j_a for a truncated lattice with $\Lambda_j = 1/2$. The circuit elements appearing in this circuit are the Hadamard, CNOT, and Z-axis single-qubit rotation implementing a Z-to-X basis change, a controlled bit flip, and a relative phase, respectively.

with matrix elements serving as weights of the measured probabilities in the measurement of the electric energy expectation value as shown in Fig. 3. The the data appearing in Fig. 3 are presented in Tables III and IV.

APPENDIX B: PLAQUETTE OPERATOR FOR $\Lambda_j = 1/2$ LATTICES OF ARBITRARY PLAQUETTE NUMBER IN ONE DIMENSION

While the circuit implementation of the plaquette operator has been shown in Fig. 2 for the two-plaquette truncated lattice with periodic boundary conditions and $\Lambda_j = 1/2$, the operator for lattices of larger size may be implemented with 14 nearest-neighbor CNOT entangling gates as shown in Fig. 4. This circuit is a massaged version of the circuit of four two-qubit-controlled $X \otimes X \otimes X$ operators with coefficients $\{1, 1/2, 1/2, 1/4\}$ for control states $|0\rangle, |1\rangle, |2\rangle, |3\rangle$ in the combined Hilbert space of j_ℓ and j_r. Just as in the main text, rotations are defined by linear combinations of $\hat{\square}^{(1/2)}$ matrix elements, as established in Ref. [48], described by the following matrix structure:

$$\vec{\beta} = \begin{pmatrix} 1 & 1 & 1 & 1 \\ 1 & -1 & -1 & 1 \\ -1 & -1 & 1 & 1 \\ -1 & 1 & -1 & 1 \end{pmatrix}^{-1} \begin{pmatrix} 1 \\ 1/2 \\ 1/2 \\ 1/4 \end{pmatrix},$$
$$\tilde{\beta} = \begin{pmatrix} 1 & 1 \\ -1 & 1 \end{pmatrix}^{-1} \begin{pmatrix} 1 \\ 1/4 \end{pmatrix}, \tag{B1}$$

such that $\vec{\beta} = (3/16, 1/16, 3/16, 9/16)$ and $\tilde{\beta} = (3/8, 5/8)$.

APPENDIX C: ALTERNATE PLAQUETTE GAUGE VARIANT COMPLETION

The optimality of the operator decomposition in the physical subspace is hardware-specific. For simple comparison to the GVC used on superconducting hardware in this work, a more naïve choice of plaquette operator implementation for the two-plaquette lattice would be to use the operator exactly as defined by the matrix elements in Eq. (6) with no modifications in the unphysical space (i.e., different charge superselection sectors). In this case, the Pauli decomposition contains eight operators

$$\hat{\square} = \left(\frac{5}{32}\mathbb{I} + \frac{3}{32}Z\right) \otimes X \otimes X \otimes X + \left(-\frac{3}{32}\mathbb{I} - \frac{5}{32}Z\right) \otimes X \otimes Y \otimes Y + \left(-\frac{5}{32}\mathbb{I} - \frac{3}{32}Z\right) \otimes Y \otimes X \otimes Y + \left(-\frac{3}{32}\mathbb{I} - \frac{5}{32}Z\right) \otimes Y \otimes Y \otimes X, \tag{C1}$$

and it remains convenient for the Trotterization that these eight operators commute. However, the number of CNOT gates required to implement this operator increases by a factor of four compared to the operator structure of Fig. 2, implemented now in four different bases

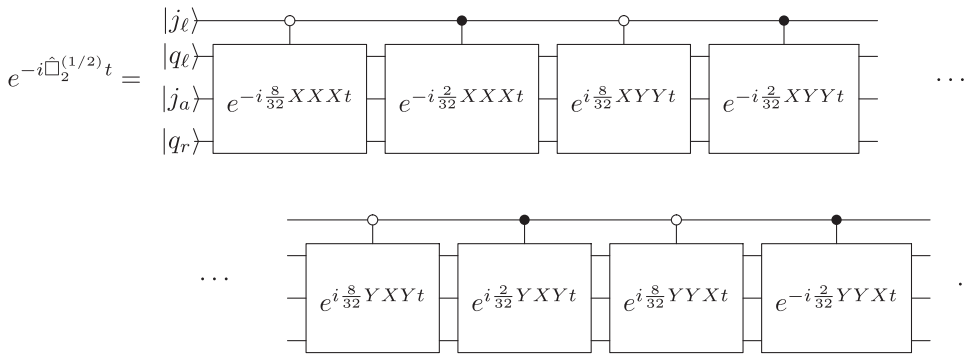

(C2)

This makes clear that the quantum resources for operator implementation depends even on the unphysical details of the calculation design—the choice of gauge invariant completion allows hardware-specific optimization leveraging this sensitivity.

[1] H. D. Politzer, Phys. Rev. Lett. **30**, 1346 (1973).
[2] D. J. Gross and F. Wilczek, Phys. Rev. Lett. **30**, 1343 (1973).
[3] H. D. Politzer, Phys. Rep. **14**, 129 (1974).
[4] S. Weinberg, Phys. Rev. Lett. **19**, 1264 (1967).
[5] S. L. Glashow, Nucl. Phys. **22**, 579 (1961).
[6] A. Salam, Conf. Proc. C **680519**, 367 (1968), https://inspirehep.net/literature/53083.
[7] P. W. Higgs, Phys. Rev. Lett. **13**, 508 (1964).
[8] K. G. Wilson, Phys. Rev. D **10**, 2445 (1974).
[9] M. Creutz, Phys. Rev. D **21**, 2308 (1980).
[10] S. P. Jordan, K. S. M. Lee, and J. Preskill, Science **336**, 1130 (2012).
[11] S. P. Jordan, K. S. M. Lee, and J. Preskill, Quantum Inf. Comput. **14**, 1014 (2014), https://inspirehep.net/literature/1082274.
[12] U.-J. Wiese, Ann. Phys. (Amsterdam) **525**, 777 (2013).
[13] U.-J. Wiese, Nucl. Phys. **A931**, 246 (2014).
[14] S. P. Jordan, K. S. M. Lee, and J. Preskill, arXiv:1404.7115.
[15] T. Pichler, M. Dalmonte, E. Rico, P. Zoller, and S. Montangero, Phys. Rev. X **6**, 011023 (2016).
[16] M. Dalmonte and S. Montangero, Contemp. Phys. **57**, 388 (2016).
[17] R. D. Somma, Quantum Inf. Comput. **16**, 1125 (2016), https://ui.adsabs.harvard.edu/abs/2015arXiv150306319S/abstract.
[18] M. C. Bañuls, K. Cichy, J. I. Cirac, K. Jansen, and S. Kühn, Phys. Rev. X **7**, 041046 (2017).
[19] E. Ercolessi, P. Facchi, G. Magnifico, S. Pascazio, and F. V. Pepe, Phys. Rev. D **98**, 074503 (2018).
[20] P. Sala, T. Shi, S. Kühn, M. C. Bañuls, E. Demler, and J. I. Cirac, Phys. Rev. D **98**, 034505 (2018).
[21] A. Macridin, P. Spentzouris, J. Amundson, and R. Harnik, Phys. Rev. Lett. **121**, 110504 (2018).
[22] J. Preskill, Proc. Sci., LATTICE2018 (**2018**) 024 [arXiv:1811.10085].
[23] D. B. Kaplan and J. R. Stryker, arXiv:1806.08797.
[24] N. Klco and M. J. Savage, Phys. Rev. A **99**, 052335 (2019).
[25] D. C. Hackett, K. Howe, C. Hughes, W. Jay, E. T. Neil, and J. N. Simone, Phys. Rev. A **99**, 062341 (2019).
[26] I. Raychowdhury and J. R. Stryker, arXiv:1812.07554.
[27] A. Bazavov, S. Catterall, R. G. Jha, and J. Unmuth-Yockey, Phys. Rev. D **99**, 114507 (2019).
[28] A. Alexandru, P. F. Bedaque, S. Harmalkar, H. Lamm, S. Lawrence, and N. C. Warrington (NuQS Collaboration), Phys. Rev. D **100**, 114501 (2019).
[29] E. Zohar, J. I. Cirac, and B. Reznik, Phys. Rev. Lett. **109**, 125302 (2012).
[30] E. Zohar, J. I. Cirac, and B. Reznik, Phys. Rev. Lett. **110**, 125304 (2013).
[31] D. Banerjee, M. Dalmonte, M. Muller, E. Rico, P. Stebler, U. J. Wiese, and P. Zoller, Phys. Rev. Lett. **109**, 175302 (2012).
[32] D. Banerjee, M. Bögli, M. Dalmonte, E. Rico, P. Stebler, U. J. Wiese, and P. Zoller, Phys. Rev. Lett. **110**, 125303 (2013).
[33] D. Marcos, P. Widmer, E. Rico, M. Hafezi, P. Rabl, U. J. Wiese, and P. Zoller, Ann. Phys. (Amsterdam) **351**, 634 (2014).
[34] L. García-Álvarez, J. Casanova, A. Mezzacapo, I. L. Egusquiza, L. Lamata, G. Romero, and E. Solano, Phys. Rev. Lett. **114**, 070502 (2015).
[35] A. Mezzacapo, E. Rico, C. Sabín, I. L. Egusquiza, L. Lamata, and E. Solano, Phys. Rev. Lett. **115**, 240502 (2015).
[36] A. Bazavov, Y. Meurice, S.-W. Tsai, J. Unmuth-Yockey, and J. Zhang, Phys. Rev. D **92**, 076003 (2015).
[37] E. Zohar, J. I. Cirac, and B. Reznik, Rep. Prog. Phys. **79**, 014401 (2016).
[38] K. Marshall, R. Pooser, G. Siopsis, and C. Weedbrook, Phys. Rev. A **92**, 063825 (2015).
[39] E. Zohar, A. Farace, B. Reznik, and J. I. Cirac, Phys. Rev. A **95**, 023604 (2017).
[40] A. Bermudez, G. Aarts, and M. Müller, Phys. Rev. X **7**, 041012 (2017).

[41] T. V. Zache, F. Hebenstreit, F. Jendrzejewski, M. K. Oberthaler, J. Berges, and P. Hauke, Sci. Technol. **3**, 034010 (2018).
[42] J. Zhang, J. Unmuth-Yockey, J. Zeiher, A. Bazavov, S. W. Tsai, and Y. Meurice, Phys. Rev. Lett. **121**, 223201 (2018).
[43] E. Gustafson, Y. Meurice, and J. Unmuth-Yockey, Phys. Rev. D **99**, 094503 (2019).
[44] Z. Davoudi, M. Hafezi, C. Monroe, G. Pagano, A. Seif, and A. Shaw, arXiv:1908.03210.
[45] E. A. Martinez, C. A. Muschik, P. Schindler, D. Nigg, A. Erhard, M. Heyl, P. Hauke, M. Dalmonte, T. Monz, P. Zoller, and R. Blatt, Nature (London) **534**, 516 (2016).
[46] N. Klco, E. F. Dumitrescu, A. J. McCaskey, T. D. Morris, R. C. Pooser, M. Sanz, E. Solano, P. Lougovski, and M. J. Savage, Phys. Rev. A **98**, 032331 (2018).
[47] H.-H. Lu, N. Klco, J. M. Lukens, T. D. Morris, A. Bansal, A. Ekström, G. Hagen, T. Papenbrock, A. M. Weiner, M. J. Savage, and P. Lougovski, Phys. Rev. A **100**, 012320 (2019).
[48] N. Klco and M. J. Savage, arXiv:1904.10440.
[49] K. Yeter-Aydeniz, E. F. Dumitrescu, A. J. McCaskey, R. S. Bennink, R. C. Pooser, and G. Siopsis, Phys. Rev. A **99**, 032306 (2019).
[50] C. Kokail *et al.*, Nature (London) **569**, 355 (2019).
[51] J. Kogut and L. Susskind, Phys. Rev. D **11**, 395 (1975).
[52] The space referred to as unphysical can be naturally interpreted as isolated Hilbert spaces with nonzero external sources.
[53] J. Preskill, Quantum **2**, 79 (2018).
[54] C. Muschik, M. Heyl, E. Martinez, T. Monz, P. Schindler, B. Vogell, M. Dalmonte, P. Hauke, R. Blatt, and P. Zoller, New J. Phys. **19**, 103020 (2017).
[55] S. A. Chin, O. S. van Roosmalen, E. A. Umland, and S. E. Koonin, Phys. Rev. D **31**, 3201 (1985).
[56] G. Burgio, R. De Pietri, H. A. Morales-Tecotl, L. F. Urrutia, and J. D. Vergara, Nucl. Phys. **B566**, 547 (2000).
[57] M. Mathur, J. Phys. A **38**, 10015 (2005).
[58] M. Mathur, Phys. Lett. B **640**, 292 (2006).
[59] T. Byrnes and Y. Yamamoto, Phys. Rev. A **73**, 022328 (2006).
[60] R. Anishetty, M. Mathur, and I. Raychowdhury, J. Phys. A **43**, 035403 (2010).
[61] P. Orland, Proc. Sci., LATTICE2013 (**2014**) 330 [arXiv:1311.4192].
[62] K. Stannigel, P. Hauke, D. Marcos, M. Hafezi, S. Diehl, M. Dalmonte, and P. Zoller, Phys. Rev. Lett. **112**, 120406 (2014).
[63] M. Rizzi, Proc. Sci., QCD-TNT-III2013 (**2013**) 036.
[64] R. Anishetty and I. Raychowdhury, Phys. Rev. D **90**, 114503 (2014).
[65] E. Zohar and M. Burrello, Phys. Rev. D **91**, 054506 (2015).
[66] Y. Kuno, K. Kasamatsu, Y. Takahashi, I. Ichinose, and T. Matsui, New J. Phys. **17**, 063005 (2015).
[67] Y. Liu and R. Liu, Sci. China Phys. Mech. Astron. **57**, 2259 (2014).
[68] Y.-X. Hu, C. Miniatura, D. Wilkowski, and B. Gremaud, Phys. Rev. A **90**, 023601 (2014).
[69] L. Tagliacozzo, A. Celi, and M. Lewenstein, Phys. Rev. X **4**, 041024 (2014).
[70] Y. Kuno, S. Sakane, K. Kasamatsu, I. Ichinose, and T. Matsui, Phys. Rev. D **95**, 094507 (2017).
[71] E. Zohar and J. I. Cirac, Phys. Rev. B **98**, 075119 (2018).
[72] J. Bender, E. Zohar, A. Farace, and J. I. Cirac, New J. Phys. **20**, 093001 (2018).
[73] P. Dreher, Proc. Sci., LATTICE2018 (**2018**) 036 [arXiv:1811.01309].
[74] J. R. Stryker, Phys. Rev. A **99**, 042301 (2019).
[75] D.-S. Li, C.-W. Wu, M. Zhong, W. Wu, and P.-X. Chen, arXiv:1810.09213.
[76] E. Zohar, in *Tensor Network and entanglement Florence, Italy, 2018*, SciPost Physics Lecture Notes Vol. 12 (2020), https://scipost.org/SciPostPhysLectNotes.12.
[77] H. Lamm, S. Lawrence, and Y. Yamauchi (NuQS Collaboration), Phys. Rev. D **100**, 034518 (2019).
[78] E. Zohar and J. I. Cirac, Phys. Rev. D **99**, 114511 (2019).
[79] A. M. Polyakov, Phys. Lett. **82B**, 247 (1979).
[80] S. Mandelstam, Phys. Rev. D **19**, 2391 (1979).
[81] Y. Nambu, Phys. Lett. **80B**, 372 (1979).
[82] A. M. Polyakov, Nucl. Phys. **B164**, 171 (1980).
[83] W. Furmanski and A. Kolawa, Nucl. Phys. **B291**, 594 (1987).
[84] R. Gambini, L. Leal, and A. Trias, Phys. Rev. D **39**, 3127 (1989).
[85] C. Di Bartolo, R. Gambini, and L. Leal, Phys. Rev. D **39**, 1756 (1989).
[86] R. Anishetty and H. S. Sharatchandra, Phys. Rev. Lett. **65**, 813 (1990).
[87] B. Bruegmann, Phys. Rev. D **43**, 566 (1991).
[88] N. J. Watson, Phys. Lett. B **323**, 385 (1994).
[89] I. Raychowdhury, Eur. Phys. J. C **79**, 235 (2019).
[90] D. Horn, Phys. Lett. **100B**, 149 (1981).
[91] P. Orland and D. Rohrlich, Nucl. Phys. **B338**, 647 (1990).
[92] S. Chandrasekharan and U. J. Wiese, Nucl. Phys. **B492**, 455 (1997).
[93] R. Brower, S. Chandrasekharan, and U. J. Wiese, Phys. Rev. D **60**, 094502 (1999).
[94] L. Tagliacozzo, A. Celi, P. Orland, and M. Lewenstein, Nat. Commun. **4**, 2615 (2013).
[95] Y. Meurice, A. Bazavov, S.-W. Tsai, J. Unmuth-Yockey, L.-P. Yang, and J. Zhang, Proc. Sci., LATTICE2016 (**2016**) 325 [arXiv:1611.08711].
[96] R. Brower, *Formulating lattice field theory for a quantum computer*, Intersection of QIS/HEP (Aspen Center for Physics, 2019), https://indico.hep.caltech.edu/event/184/attachments/188/244/Aspen QC brower.pdf.
[97] Y. Meurice, *Quantum field theory with cold atoms*, Intersection of QIS/HEP (Aspen Center for Physics, 2019), https://indico.hep.caltech.edu/event/184/attachments/188/236/meuriceaspen19.pdf.
[98] 20-qubit backend: IBM Q team, IBM Q 20 Tokyo backend specification V1.2.5 with qiskit V0.11.0 (2019).
[99] Equation (A1) shows explicitly the Hamiltonian structure with the chosen GVC. If the GVC of Eq. (6) was used without modification, a factor of four in quantum gates is expected as shown in Appendix C.
[100] The Trotter step in this calculation has been ordered in application as the first plaquette, the second plaquette as written in Eq. (8), and lastly the electric time evolution operator.
[101] E. Zohar, J. I. Cirac, and B. Reznik, Phys. Rev. A **88**, 023617 (2013).